REPORT DOCUMENTATION PAGE

Form Approved
OMB No. 0704-0188

1. REPORT DATE *(DD-MM-YYYY)*	2. REPORT TYPE	3. DATES COVERED *(From - To)*
29-12-2020	Final	2/1/2017 - 9/30/2020

4. TITLE AND SUBTITLE
Charge Transfer States at Donor-Acceptor Heterojunctions: The role of morphology on dissociation efficiency and device lifetimes

5a. CONTRACT NUMBER
N00014-17-1-2211

5b. GRANT NUMBER

5c. PROGRAM ELEMENT NUMBER

6. AUTHOR(S)
Forrest, Stephen R., Principal Investigator

5d. PROJECT NUMBER

5e. TASK NUMBER

5f. WORK UNIT NUMBER

7. PERFORMING ORGANIZATION NAME(S) AND ADDRESS(ES)
The Regents of the University of Michigan
3003 S. State Street
Ann Arbor, MI 48109-1274

8. PERFORMING ORGANIZATION REPORT NUMBER

9. SPONSORING/MONITORING AGENCY NAME(S) AND ADDRESS(ES)
ONR Naval Materials Div
875 N. Randolph Street
Arlington, VA 22203-1995

10. SPONSOR/MONITOR'S ACRONYM(S)

11. SPONSOR/MONITOR'S REPORT NUMBER(S)

12. DISTRIBUTION/AVAILABILITY STATEMENT
Approved for public release; distribution is unlimited

13. SUPPLEMENTARY NOTES

14. ABSTRACT
The generation of photocurrent at organic donor-acceptor (D-A) junctions occurs via formation of a charge transfer (CT) exciton, aka the polaron pair (PP). The exciton generated by optical absorption diffuses to the D-A junction where it's driven into the CT state Coulombically bound across the heterojunction (HJ). This "indirect" PP state is a precursor to the free charge separated (CS) state resulting in photocurrent in the external circuit. This program goals: understanding CT state photophysics & its dependence on donor & acceptor materials combinations & film morphology; achieve ~100% internal quantum efficiency at small molecule D-A junctions; find relationship between device lifetime/photophysical properties.

15. SUBJECT TERMS
nanomorphology, photogeneration process, bi-ternary organic photovoltaics, molecular alloys, non-fullerene acceptors

16. SECURITY CLASSIFICATION OF:			17. LIMITATION OF ABSTRACT	18. NUMBER OF PAGES	19a. NAME OF RESPONSIBLE PERSON
a. REPORT	b. ABSTRACT	c. THIS PAGE			Eva Ruff
U	U	U	UU	21	19b. TELEPHONE NUMBER *(Include area code)* 734-764-1533

Final Report

Project Title:	Charge Transfer States at Donor-Acceptor Heterojunctions: The role of morphology on dissociation efficiency and device lifetimes
Project Period:	2/1/2017 – 9/30/2020
Submission Date:	12/29/2020
Recipient:	University of Michigan
Recipient DUNS #:	073133571
Address:	3003 S. State Street, Ann Arbor, MI 48109-1274
Website:	www.umich.edu/~ocm/
Award Number:	N00014-17-1-2211
Awarding Agency:	Office of Naval Research
Principal Investigator:	Stephen Forrest Principal Investigator Phone: 734-647-1147 Email: stevefor@umich.edu
Submitted by: **(if other than PI)**	Eva Ruff Administrative Assistant Senior Phone: 734-764-1533 Email: emruff@umich.edu
DOE Contracting Officer:	Angela Carey, angela.l.carey@navy.mil
ONR Project Manager:	James Paul Armistead, paul.armistead@navy.mil

Eva Ruff 12/29/20

Signature **Date**

Major Goals

The generation of photocurrent at organic donor-acceptor (D-A) junctions occurs via formation of a charge transfer (CT) exciton, also known as the polaron pair (PP). The exciton generated by optical absorption diffuses to the D-A junction where it is driven into the CT state that is Coulombically bound across the heterojunction (HJ). This "indirect" PP state is a precursor to the free charge separated (CS) state that results in photocurrent in the external circuit.

Given the centrality of its importance in the photogeneration process, it is essential that the formation of PPs be understood and controlled. This understanding should lead to the development of D-A systems and film morphologies capable of achieving 100% internal quantum efficiency across the visible and near infrared (NIR) spectral regions. Our group at the University of Michigan has played a pioneering role in understanding such states, developing fundamental quantum and semi-classical theories that determine their static and dynamic properties, with special attention to the effects that local and global film morphology have on the CT state dissociation process.[1-3] In this program, we extend our theoretical and experimental approaches to gain a comprehensive understanding of CT state photophysics and its dependence on donor and acceptor materials combinations (*including non-fullerene systems*), and film morphology. We will use this understanding to achieve ~100% internal quantum efficiency (*IQE*) at small molecule D-A junctions, thus guiding our choice of materials and deposition conditions to achieve this major milestone in organic photovoltaics.

In this program we endeavor to answer the following fundamental questions:

1. *What is the role of the CT state energy in its dissociation probability, and hence its efficiency in photocurrent generation?*
2. *Is there a combination of materials and morphologies that increases the rate of dissociation vs. recombination?*
3. *What determines the donor-acceptor dilution ratio in mixed HJ active layers[4, 5] that leads to the highest efficiency?*
4. *What fundamental differences are there in the CT state dynamics of fullerene and non-fullerene acceptors?*
5. *Can the control of morphology during growth, and D-A materials compositions lead to 100% internal quantum efficiency across the visible and into the near infrared?*
6. *Can the CT state photophysics be used as an indicator of degradation processes in organic photovoltaics, and ultimately can these processes be slowed via insights gained through monitoring the properties of the CT state over time?*

[1] N. C. Giebink, B. E. Lassiter, G. P. Wiederrecht, M. R. Wasielewski, and S. R. Forrest, "The Ideal Diode Equation for Organic Heterojunctions. II. The role of polaron pair recombination," **Phys. Rev. B**, vol. 82, p. 155306, 2010.
[2] N. C. Giebink, G. P. Wiederrecht, M. R. Wasielewski, and S. R. Forrest, "The Ideal Diode Equation for Organic Heterojunctions. I. Derivation and Application," **Phys. Rev. B,** vol. 82, p. 155305, 2010.
[3] X. Liu, K. Ding, A. Panda, and S. R. Forrest, "Charge transfer states in dilute donor acceptor blend organic heterojunctions," **ACS Nano**, vol. 10, p. 7619, 2016.
[4] S. Uchida, J. Xue, B. P. Rand, and S. R. Forrest, "Organic small molecule solar cells with a homogeneously mixed copper phthalocyanine: C_{60} active layer," **Appl. Phys. Lett.**, vol. 84, p. 4218, 2004.
[5] J. Xue, B. P. Rand, S. Uchida, and S. R. Forrest, "A hybrid planar-mixed molecular heterojunction photovoltaic cell," **Adv. Mater.**, vol. 17, p. 66, 2005.

Accomplishments

I. Correlation between active layer nanomorphology and photogeneration processes

A direct correlation between nanomorphology of the mixed active layers and the photogeneration processes in DBP:C_{70} blends has been established using a combination of experimental and computational methods. The charge transfer state energy can be directly controlled by growing alternating multilayer stacks in **Fig. 1**. Excitons generated in mixed regions experience spatial confinement leading to efficient dissociation into charge transfer (CT) states with a high recombination efficiency. Excitons that dissociate at the boundary of nanocrystalline C_{70} regions efficiently form delocalized CT states. Using a quantum mechanical model, we are able to correlate the size of the nano-domains with the CT state energy, showing that the red shift with the size of domain is due to reduced quantum confinement and hence, binding energy. This relationship and the model fits (lines) are shown in **Fig. 2**.

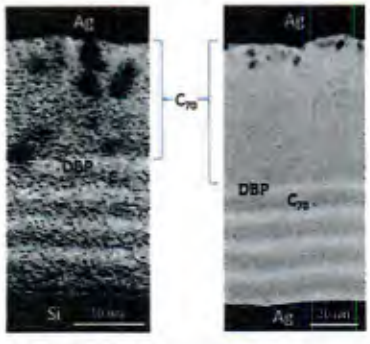

Figure 1. (a) Image of 5 pairs of 2 nm alternating layers capped by 20 nm C_{70} and 150 nm Ag. (b) Image of 5 pairs of 5 nm thick alternating layers capped by 20 nm C_{70} and a 50 nm Ag.

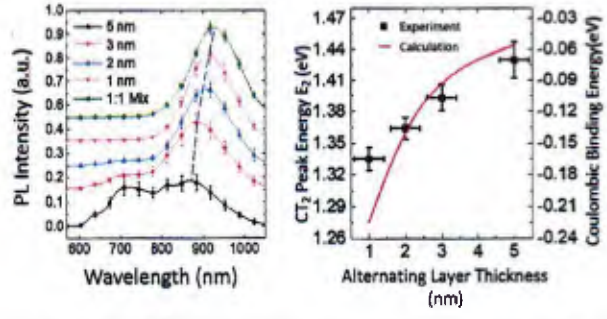

Figure 2. (left) Photoluminescence (PL) spectra of multilayer stacks consisting of alternating layers of DBP and C_{70}. (right) PL peak energies of charge transfer CT_2 states, E_2, and calculated Coulombic binding energies vs. layer thickness.

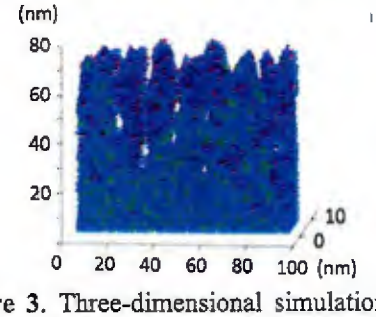

Figure 3. Three-dimensional simulation of a 1:8 DBP:C_{70} blended heterojunction (HJ). Blue areas are C_{70} molecules. Green (red) areas are DBP molecules that form (do not form) percolating paths to the anode.

A Monte Carlo simulation model is used to understand the charge collection process in mixed heterojunctions (HJs) with low donor concentrations. The planar and high aspect ratio DBP molecules readily form continuous and extended percolating paths as in **Fig. 3**, allowing for the extraction of photogenerated charges at the opposing electrodes that are positioned exceptionally large distances from their point of origin. Combined with the larger absorption coefficient of DBP compared with C_{70} explains why optimized organic photovoltaics (OPV) efficiencies are obtained in such a dilute donor system. The molecular dynamics model used to "construct" these model morphologies also predict the observed shifts in blend with good accuracy.

We also extended our energy studies to non-fullerene systems. In particular, A-D-A large fused rings with relatively high electron affinities and planar molecular structures. We

demonstrated a highly efficient ternary near-infrared (NIR) absorbing solar cell with a polymer donor (PCE-10) and two NIR-absorbing non-fullerene acceptors (NFAs) (BT-CIC and TT-FIC). The optimized PCE-10:BT-CIC:TT-FIC based single junction cell exhibits power conversion efficiency (*PCE*) = 12.6±0.3% with the short-circuit current density (J_{SC}) of 25.5 mA cm^{-2} and the voltage loss of 0.55 V, as shown in **Fig. 4**. Using binary NFA devices in a tandem cell we obtained an efficiency of 15% and with the ternary cells, 15.4% under 1 sun, AM1.5G simulated solar illumination. To our knowledge these are both record efficiencies for OPVs at this time.

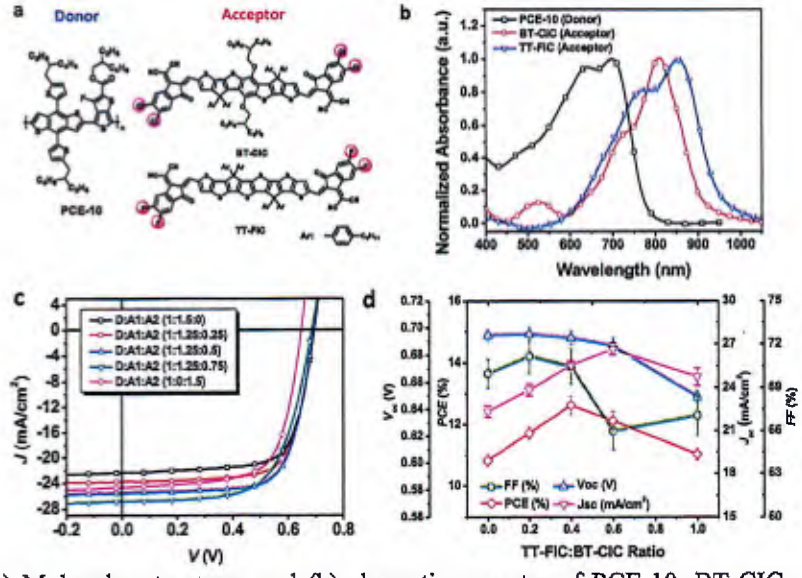

Figure 4. (a) Molecular structures and (b) absorption spectra of PCE-10, BT-CIC and TT-FIC. (c) Current density-voltage (*J-V*) characteristics of ternary organic photovoltaic (OPV) cells based on the three molecules. (d) Open-circuit voltage (V_{OC}), short-circuit current density (J_{SC}) and fill factor (*FF*) of ternary cells as a function of TT-FIC:BT-CIC blend ratio.

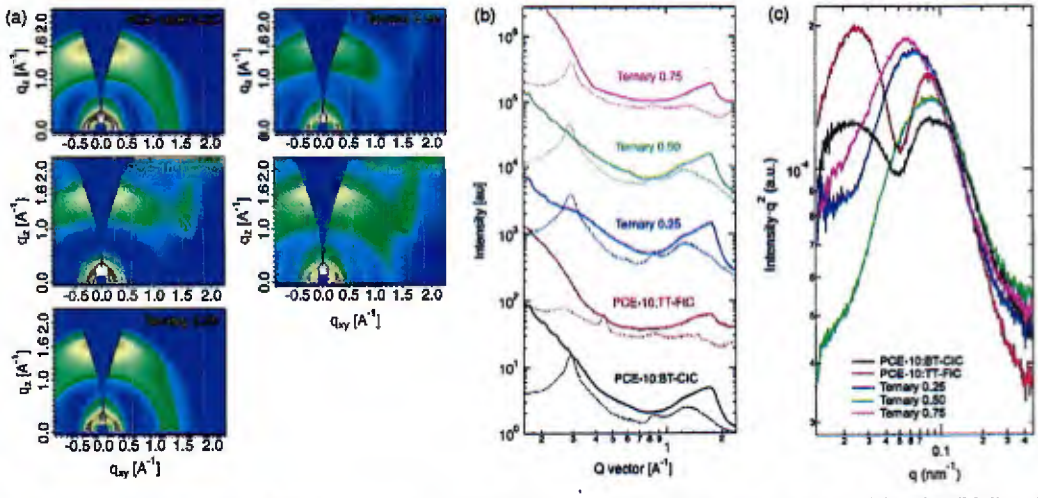

Figure 5. (a) 2D glancing incidence x-ray diffraction patterns of binary and ternary blends. (b) In-plane (dotted line) and out-of-plane (solid line) x-ray scattering patterns. (c) Resonant soft x-ray diffraction of binary and ternary blends.

The reduced phase separation in ternary blends increases the interfacial area between donors and acceptors, thus promoting exciton dissociation and giving rise to improved J_{SC}. Soft x-ray and glancing incidence x-ray diffraction in **Fig. 5** provide insight into the phase separation that we have learned to control to obtain the highest charge extraction efficiencies.

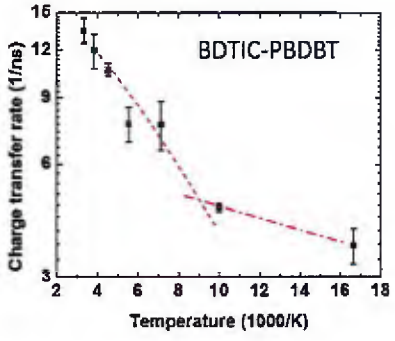

Figure 6. Temperature dependent charge transfer rate of BDTIC-PBDBT HJ.

Additionally, we find that our devices show efficient charge generation upon small driving energies, traditionally believed to be necessary to split the strongly bound excitons at the D:A interfaces, constitutes an additional voltage loss for OPV. This efficient charge separation, even with a small driving force, is benefited from the small Urbach energy E_U, (corresponding to a reduced energetic disorder) of the blend.

The temperature dependent charge transfer rate shown in **Fig. 6** suggests that charge transfer at donor-acceptor HJ is governed by Marcus transfer at temperatures above 120K, while tunneling transfer dominates at lower temperatures. Fullerene derivatives and different NFAs were paired with a group of donor molecules, to vary the energy offset (ΔE_{CT}) between the acceptor exciton and CT state to between 0 and 0.6 eV. The optimal ΔE_{CT}, i.e., CT energy loss of the exciton generated in the acceptor is where the CT rate is maximized. An example of a non-fullerene acceptor, BT-IC showed a CT energy loss of only $\Delta E_{CT} = -0.25 \pm 0.10$ eV, which was significantly less than for the fullerenes, as shown in **Fig. 7**. Furthermore, we found a correlation between the optimal ΔE_{CT} and the exciton binding energy (E_B). As shown in **Figs. 8 and 9**, using density functional theory (DFT), the relationship between E_B and molecular geometry as well as the electron-donating/extraction strength of the molecule were analyzed, leading to a comprehensive quantum mechanical model associating molecular structure to energy loss.

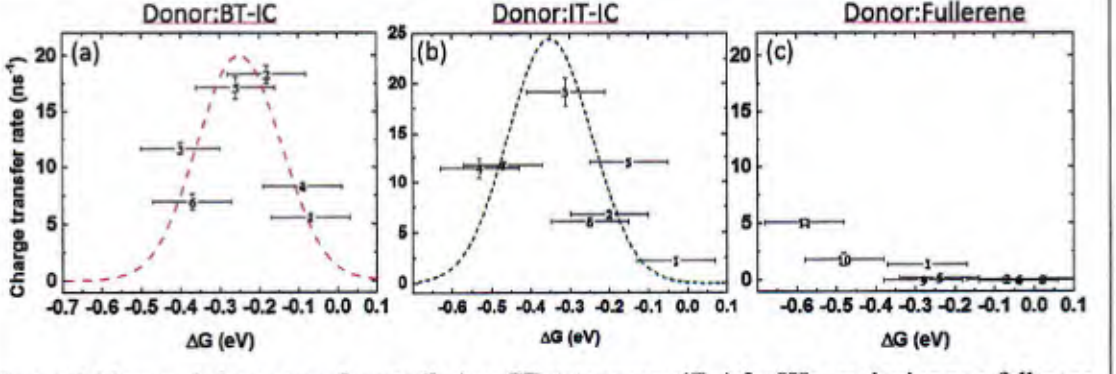

Figure 7. Measured charge transfer rate (k_{CT}) vs CT state energy (E_{CT}) for HJs employing non-fullerene acceptors (NFAs) and fullerene derivatives acceptors.

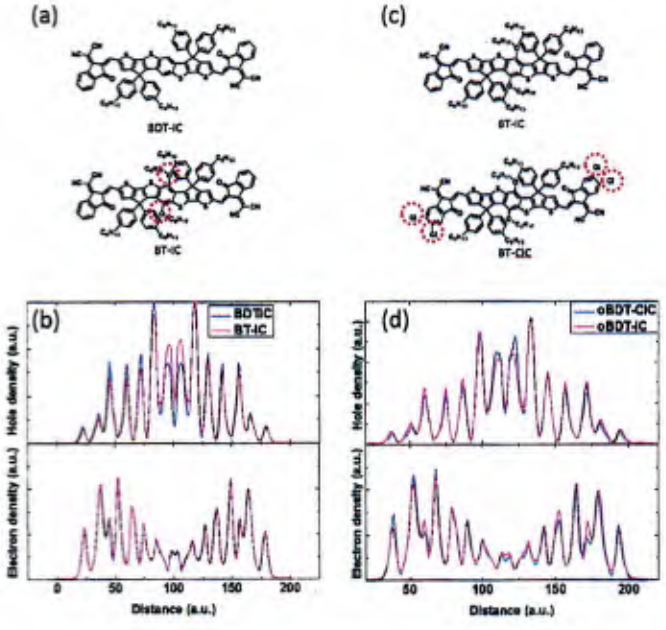

Figure 8. Electron and hole density profile of four NFA molecules.

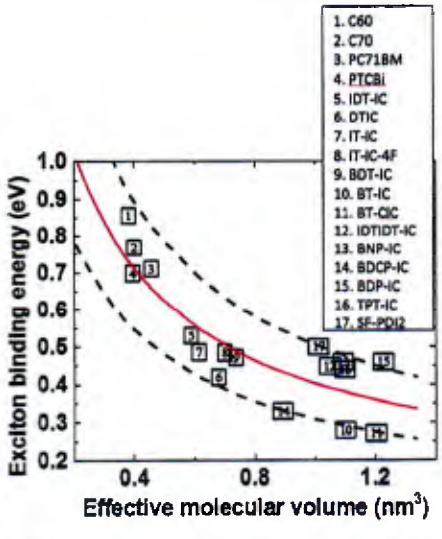

Figure 9. Exciton binding energy, E_B, found via density functional theory (DFT) vs effective molecular volume for several acceptor molecules indicated in legend. The red solid line is a fit assuming electron confinement within the effective molecular volume for each molecule. The calculation assumes a dielectric parameter, f = 5.4. The area within the dotted lines is the 95% confidence band.

II. Bi-ternary organic photovoltaics

Most ternary OPVs exhibit inferior performance to analogous binary OPVs that is due, in part, to difficulties in optimizing the morphology of three-component active regions. Additionally, the choice of the third component is restricted to compounds that ensure efficient charge transfer between the molecules within the active layer. Furthermore, when the active region comprises two donors and one acceptor, the open-circuit voltage (V_{OC}) of the ternary OPV is generally always limited by the shallower of the two highest occupied molecular orbital (HOMO) of the donors, since holes are likely to transfer to higher energy levels prior to extraction at the anode (see **Fig. 10(a) & (d)**). This limits V_{OC} and, therefore, the *PCE* attainable employing ternary component OPVs.

Here, we introduced a new called a bi-layer ternary OPV (or *bi-ternary*) OPV. This vacuum thermally evaporated device comprises two individual binary bulk HJs fused at a planar junction as shown in **Fig. 10(b) & (c)**. The stacked sub-elements contain two different donor molecules (iBuBDTC and DTDCPB) but share a common, fullerene acceptor. This device is analogous to a tandem cell, where the charge generation layer between sub-elements is eliminated since the common acceptor allows for uninterrupted transport of photogenerated electrons across the active region. Since iBuBDTC and DTDCPB have different HOMO energies (E_{HOMO}), there are two different possible binary stacking arrangements in the bi-ternary. The first configuration is to place the DTDCPB:C_{70} segment with the higher E_{HOMO} closest to the anode. As a result, holes encounter a cascade energy landscape as shown in **Fig. 10(e)**, and are likely to exothermically transfer from iBuBDTC to DTDCPB to the anode. This bi-ternary configuration is denoted type-1 (or "right way"). The opposite stacking order corresponds to a type-2 (or "wrong way") bi-ternary (see **Fig. 10(f)**).

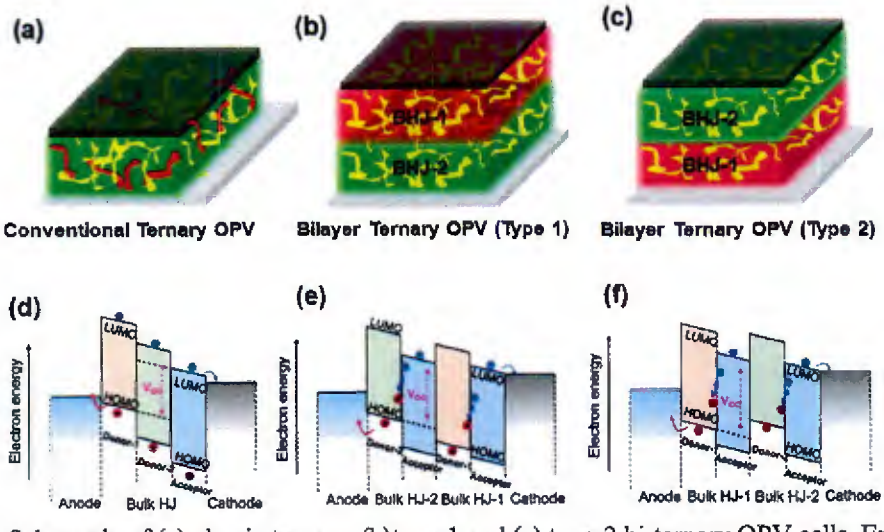

Figure 10. Schematic of (a) classic ternary, (b)type-1 and (c) type-2 bi-ternary OPV cells. Energy level diagram of (d) classic ternary. (e) type-1 and (f) type-2 bi-ternary OPV cells.

Contrary to expectations, higher performance ($PCE = 10.6 \pm 0.3\%$ *vs.* $PCE = 9.6 \pm 0.3\%$) is obtained when there is an apparent energy barrier to holes interposed by the binary sub-element between the anode and the second sub-element (i.e. the wrong way bi-ternary). This is explained from measurements of E_{HOMO} of the donors obtained by both the cyclic voltammetry and ultraviolet photoelectron spectroscopy, each of which showed that the HOMO level of iBuBDTC

is deeper than that of DTDCPB. In the wrong way device, the holes are forced to hop back from DTDCPB to the deeper E_{HOMO} of iBuBTDC. In **Fig. 11**, it is apparent that placing iBuBTDC adjacent to the anode presents a 100 meV energy barrier to hole transport, which presumably would increase charge recombination and decrease J_{SC} and *FF*. However, holes cascade from the HOMO of DTDCPB to iBuBTDC without hindrance, suggesting the absence of such a barrier.

To understand the source of this phenomenon, the energy-level alignment at the interfaces of the two HJs comprising the bi-ternary were investigated by ultraviolet photoelectron spectroscopy (UPS). Surprisingly, As shown in **Fig. 11**, the E_{HOMO} of the donors undergo a shift of 0.22 ± 0.09 eV for DTDCPB in the DTDCPB:C_{70} blend, and 0.13 ± 0.09 eV for iBuBTDC in the iBuBDTC:C_{70} blend. The energy barrier that otherwise would exist between the HOMOs of iBuBTDC and DTDCPB is eliminated, allowing holes to efficiently transport between the donors at the iBuBDTC:C_{70} and DTDCPB:C_{70} interface regardless of whether the bi-ternary of is in the type 1 or 2 configuration.

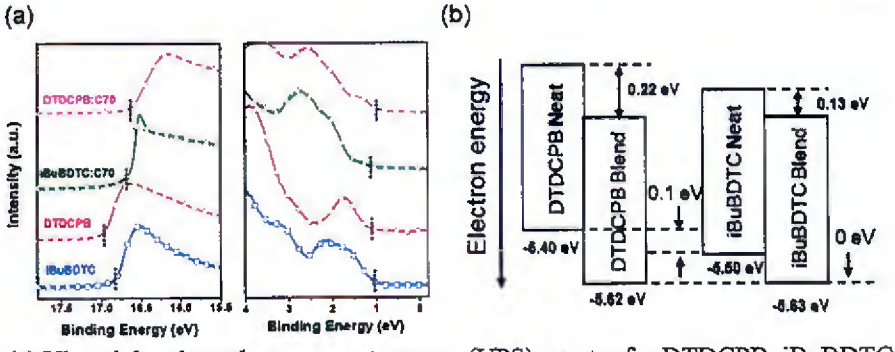

Figure 11. (a) Ultraviolet photoelectron spectroscopy (UPS) spectra for DTDCPB, iBuBDTC neat film as well as mixed blends with C_{70}. (b) Energy-level diagram extracted from UPS measurements on DTDCPB, iBuBDTC neat film and mixed blends with C_{70}.

Additionally, unlike the V_{OC} of a ternary cell that lies between that of the two binaries, the bi-ternary stacking order can be adjusted to give the highest possible V_{OC} and hence, *PCE*. As a result, optimized bi-ternary OPVs show improved performance compared to the two constituent binary devices, achieving *PCE* = 10.6 ± 0.3% under AM 1.5G 1 sun (100 mW/cm^2) simulated illumination, with V_{OC} = 0.94 ± 0.01 V, a short circuit current density of J_{sc} = 16.0 ± 0.5 mA cm^{-2}, and a fill factor (*FF*) = 0.70 ± 0.01. To our knowledge is the highest *PCE* reported for a vacuum deposited OPV.

III. Molecular alloys: Do such materials exist?

In inorganic materials, an alloy is commonly understood to be a physical mixture of two or more constituents with variable proportions that exhibits electronic and/or physical properties different from its components. Its characteristics derive almost entirely from the strong chemical bonds between atoms in the mixture. In contrast, organic materials are bonded by far weaker, electrostatic van der Waals forces. It has been proposed that in some cases these weakly bonded organic mixtures form a new substance which is called a "molecular alloy". Although there has been frequent mention of molecular organic alloys over many decades, no uniform framework has been developed to clearly define what is meant by this term. Based on the nature of chemical bonds, we propose the criteria that must be met to unambiguously identify a molecular organic alloy: that is, a mixture of two or more molecular organic substances that have intermolecular electron coupling that results in modification of the electronic states of the constituent molecules.

Specifically, we investigated the P3HT:(ICBA:$PC_{61}BM$) ternary system which has previously been proposed to form molecular alloy between the two acceptors in the blend. Evidence for the existence of an alloy was based on the observed dependence of the CT state absorption energy on the blend ratio. Analysis of the UPS data in **Fig. 12(a)** indicates that the E_{HOMO} for ICBA and the blends is at -5.8±0.1eV, and for $PC_{61}BM$ the HOMO energy is at -6.0± 0.1eV. There is no evidence found for the emergence of new ground state. The steady-state photoluminescence (PL) data in **Fig. 12(b)** show that the exciton energies of the acceptor blends are also the same as for ICBA, nor does the exciton lifetime extracted from time-resolved PL in **Fig. 12(c)** depend on the blend ratio. Thus, the excited states in the acceptor blends also do not appear to be influenced by the mixture composition.

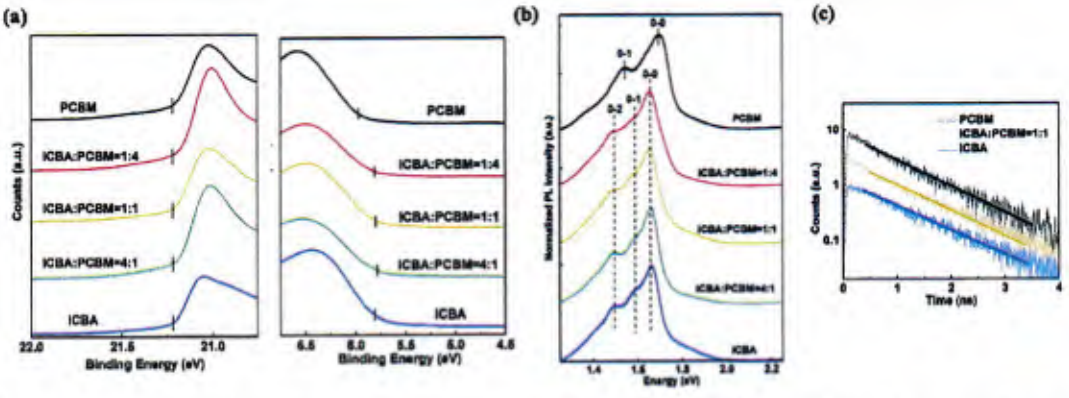

Figure 12. (a) UPS and (b) PL spectra, and (c) time-resolved PL of ICBA, PCBM and their blends.

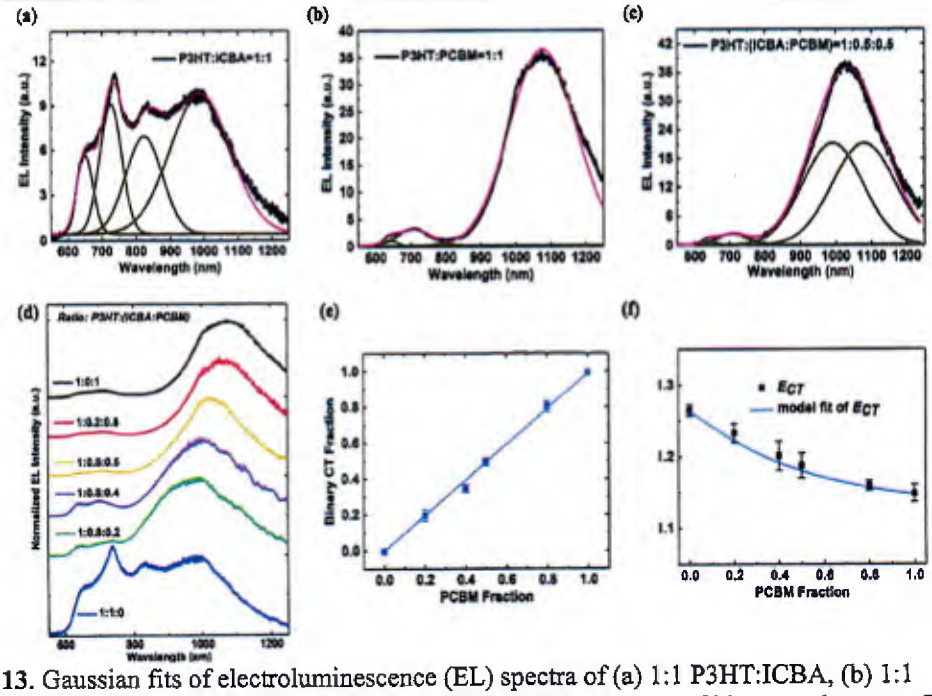

Figure 13. Gaussian fits of electroluminescence (EL) spectra of (a) 1:1 P3HT:ICBA, (b) 1:1 P3HT:PCBM and (c) 1:(0.5:0.5) P3HT:(ICBA:PCBM). (d) EL spectra of binary and ternary OPVs with different blend ratios. (e) Relationship between P3HT:PCBM CT state fraction vs. PCBM fraction. (f) CT state energy vs. PCBM fraction.

To investigate the CT states, we used a series of Gaussians to fit the electroluminescence (EL) spectra of binary and ternary OPVs. The CT state EL spectrum in **Fig. 13(c)** for a 1:(0.5:0.5) P3HT:(ICBA:$PC_{61}BM$) blend does not exhibit spectral features independent of those of the individual binaries, which are shown in **Fig. 13(a) and (b)**. A similar fitting procedure is applied to the EL spectra in **Fig. 13(d)**, for the P3HT:(ICBA:$PC_{61}BM$) junctions with different acceptor blend ratios. As presented in **Fig. 13(e)**, We find a linear relationship between the fraction of P3HT:$PC_{61}BM$ CT state emission and the $PC_{61}BM$ blend fraction. In **Fig. 13(f)** we simulate the sum of Gaussian distributions representing the two binary CT states. The simulation indicates that the linear superposition of these two Gaussian distributions results in an identical extrapolative dependence found by Vegard's Law. The previously observed bowing, or nonlinearity arises from the simple addition of the two, Gaussian-shaped CT emission spectra.

Since the totality of our measurements show no evidence for the emergence of new electronic states, we conclude that there is no existence of a molecular alloy in the P3HT:ICBA:$PC_{61}BM$ active region. Indeed, based on our criteria stated above, we find no clear example has yet been found for the existence of a molecular organic alloy.

IV. Investigation of charge transfer at the anode/active layer to reduce energy loss at interface

We studied an archetype bulk heterojunction (BHJ) comprising DBP as the donor and C_{70} as the acceptor, along with several commonly used anode buffer layers (ABL) including MoO_x, PEDOT:PSS and HAT-CN. We find that for MoO_x and PEDOT:PSS, there is frontier energy level bending near the active region/ABL interface that leads to energy losses. By independently controlling the donor/acceptor (D/A) ratio of the thin anode interface layer (AIL) at the active region/ABL interface, as the structure shown in **Fig. 14(a)**, V_{oc} can be varied over a range of 120 ± 10 mV independent of the J_{sc} and *FF*.

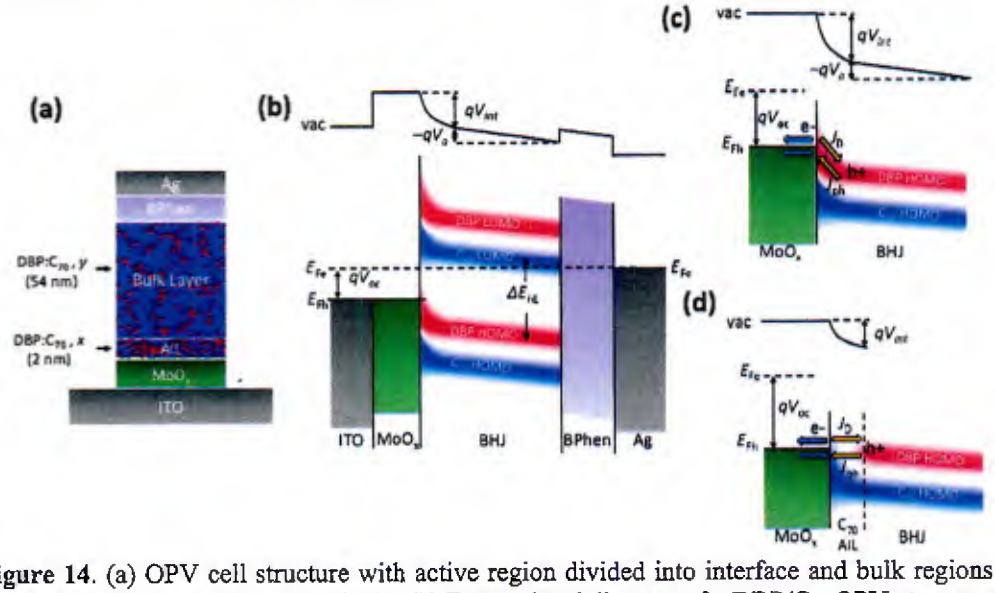

Figure 14. (a) OPV cell structure with active region divided into interface and bulk regions with C_{70} concentrations of x and y, respectively. (b) Energy level diagram of a DBP/C_{70} OPV at open circuit. (c) Energy level diagram near the interface between a DBP/C_{70} mixed layer and MoO_x at open circuit. (d) Energy level diagram near the interface between a DBP/C_{70} mixed layer and MoO_x at open circuit when a 2-nm-thick neat C_{70} anode interface layer (AIL) is inserted between the bulk layer and the MoO_x.

Figure 14(b) shows the energy level diagram of the OPV at open circuit. We assume the hole quasi-Fermi level E_{Fh} is at δ_1 above the DBP HOMO level on the anode side, E_{DBP}, and electron quasi-Fermi level E_{Fe} is at δ_2 below the C_{70} lowest unoccupied molecular orbital (LUMO) level on the cathode side, E_{C70}. Note δ_1 and δ_2 can be either positive or negative based on the energy alignment on the interfaces. Then E_{DBP} and E_{C70} have following relationship:

$$E_{DBP} = E_{C70} - \Delta E_{HL} - qV_a + qV_{int} \quad (1)$$

where ΔE_{HL} is the energy offset between C_{70} LUMO and DBP HOMO, V_a is the voltage drop across the bulk (active) layer, V_{int} is the voltage drop across the AIL due to the presence of a static interface dipole and q is the elementary charge. Note that the direction of V_{int} is defined as opposite to that of V_a and the external device voltage, V, by convention. Therefore, V is:

$$qV = E_{Fe} - E_{Fh} = (E_{C70} - \delta_2) - (E_{DBP} + \delta_1) = \Delta E_{HL} - \delta_2 - \delta_1 + qV_a - qV_{int} \quad (2)$$

Figure 14(c) shows the energy level diagram near the active region/ABL interface, with the electron and hole currents represented by blue and yellow arrows, respectively. When forward-biased, electrons transfer from the organic HOMO into MoO_x, leaving holes in the organic that flow into the BHJ and recombine with electrons injected from cathode. This is the dark current, J_D. Under illumination, a photocurrent, J_{ph}, generated in the active region flows through the ABL interface where photogenerated holes recombine with electrons in the MoO_x. While J_D depends on both the interface and bulk properties, J_{ph} depends primarily on recombination in the bulk, provided that interface recombination is insignificant. Under open-circuit conditions, $J_D = -J_{ph}$ and the total current is zero.

Because the BHJ blend morphology is isotropic, photogenerated charges require the guidance of the electric field in the BHJ to reach the electrodes. The direction of J_{ph} is decided by the sign of V_a. Thus it follows that when $V_a = 0$, then $J_{ph} = 0$. Assuming the current dependences of δ_1, δ_2 and V_{int} are small, Eq. (2) becomes:

$$qV(J_{ph} = 0) = \Delta E_{HL} - \delta_2 - \delta_1 - qV_{int} \quad (3)$$

Then, using Eq. (2) and (3):

$$V = V(J_{ph} = 0) + V_a \quad (4)$$

This scenario suggests that reducing V_{int} may be an effective way to reduce energy losses at the active region/ABL interface. To achieve this objective, we can eliminate the DBP in the AIL, as shown in **Fig. 14(d)**. The deeper HOMO of C_{70} pins the Fermi level of MoO_x, resulting in a

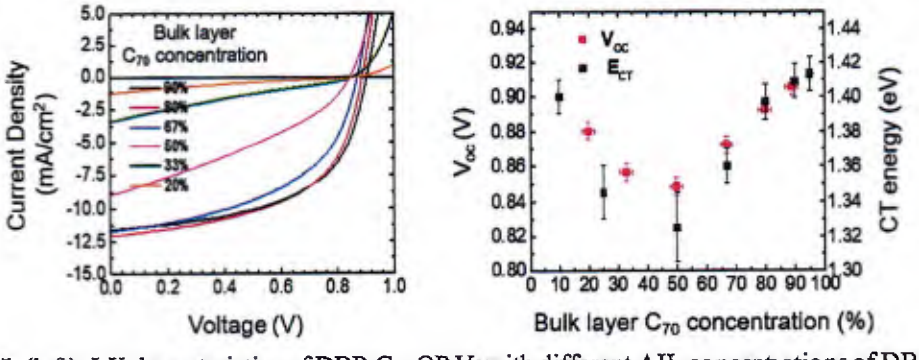

Figure 15. (left) *J-V* characteristics of DBP:C_{70} OPVs with different AIL concentrations of DBP in C_{70}. (right) V_{OC} and E_{CT} of different AIL concentrations of C_{70} in DBP.

reduced V_{int}. Hole transport between the DBP HOMO in the bulk and the C_{70} HOMO in the AIL is required to extract photogenerated holes. As long as the AIL is thin, this transport can be via tunneling and hence is *non-dissipative*. Therefore, V_{oc} will undergo a rigid shift without a change in V_a and J_{ph}.

Figure 15 shows the current density-voltage (J-V) characteristics of devices with constant AIL C_{70} concentration (x = 100%) and various values of y, with V_{OC} shown in the right of **Fig. 15** (squares) along with CT-state energies acquired from their PL spectra (diamonds). V_{OC} and the CT exciton energy have similar dependences on y, both showing a minimum near y = 50%, which was previously shown to be due to the minimization of C_{70} or DBP aggregate formation.

To separate the dependences of J_D, J_{ph}, and J on voltage, we calculate J_{ph} by subtracting J_D from the total current J. As shown in **Fig. 16**, both J_D and J_{ph} feature a rigid shift relative to the device voltage, V, depending on the composition of the AIL. When plotted with reference to V_a in **Fig. 16(b)**, the J_{ph}-V_a relationships for the two devices are almost identical in the region of $J_{ph} < 0$, showing that photogeneration in the BHJs is indeed governed by V_a and is unaffected by V_{int}, in agreement with the simulations. Both devices show V_{oc} at $V_a = -0.10 \pm 0.01$ V, as denoted by the vertical dash line. The device with a C_{70} AIL has a slightly higher J_D at a given V_a, which is possibly due to a reduced hole injection barrier.

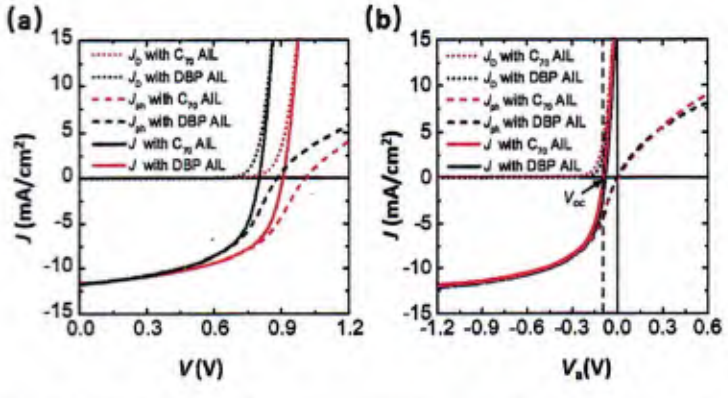

Figure 16. (a) J-V characteristics for the dark current density J_D (dotted), photocurrent density J_{ph} (dash) and total current density J (solid) of devices with a C_{70} (red), and a DBP AIL (black). (b) The same J-V characteristics as in (a) replotted with reference to voltage across the active layer, V_a. The vertical dashed line corresponds to V_{oc}.

V. Relationship between charge-transfer state electroluminescence and the degradation of organic photovoltaics

Previous research has revealed a correlation between a reduction in the V_{oc} and the CT state EL efficiency under forward bias over the course of aging of a PV cell. Other works have assumed that the external emission efficiency is equal to the EL external quantum efficiency η_{EL}. However, for an organic device where emission is dominated by the CT state, the current resulting from non-radiative recombination will be exactly zero when the emissive CT state efficiency, η_{CT}, is unity, which is not equivalent to $\eta_{EL} = 1$. For organics, CT state emission is confined to donor/acceptor junctions, thus η_{CT} can only account for nonidealities occurring within the active region. Rather, the measured EL efficiency is dependent on several factors given by:

$$\eta_{EL} = \gamma \chi_{em} \eta_{CT} \tag{5}$$

where γ is the charge balance factor. The ratio of emissive CT states formed by electrical injection, χ_{em}, depends on whether the states reside in the singlet or triplet manifold.

Under open-circuit conditions, the ideal diode equation for an OPV can be simplified as:

$$J_0\left(\exp\left(\frac{qV_{oc}}{nkT}\right) - 1\right) = -J_{ph} \tag{6}$$

where J_0 is the dark saturation current, n is the ideality factor, and J_{ph} is the photocurrent.

An OPV in thermal equilibrium requires that the photocurrent due to thermal excitation is balanced by current injection leading to recombination at the CT state. Thus, in the dark:

$$J_{out}(V_{oc}) = J_0^{rad}\left(\exp\left(\frac{qV_{oc}}{nkT}\right) - 1\right) \approx J_0^{rad}\left(\exp\left(\frac{qV_{oc}}{nkT}\right)\right), \tag{7}$$

where J_0^{rad} is the saturation current due to excitation due to a room temperature blackbody, and J_{out} is the radiative recombination current density generated from the CT state.

Returning to η_{EL}, which is defined as the number of photons emitted per electrons injected, we can write:

$$\eta_{EL} = \frac{J_{out}(V_{oc})}{J_{inj}(V_{oc})} \gamma \chi_{em} \tag{8}$$

where J_{inj} is the injected current density resulting from the applied forward voltage, which must be balanced by an equal and opposite photocurrent at V_{oc}:

$$J_{inj}(V_{oc}) = J_{ph}(V_{oc}) = J_{sc} - J_{\Delta} \tag{9}$$

Combining Eq. 7, Eq. 8, and Eq. 9, and solving for V_{oc} gives the following expressions:

$$V_{oc} = \frac{kT}{q} \ln \frac{J_{sc} - J_{\Delta}}{J_0^{rad}} + \frac{mkT}{q} \ln\left(\frac{\eta_{EL}}{\gamma \chi_{em}}\right) \tag{10}$$

$$V_{oc} = V_{oc}^{rad} + \frac{kT}{q} \ln \frac{J_{ph}(V_{oc})}{J_{sc}} + \frac{mkT}{q} \ln \eta_{CT}. \tag{11}$$

Because η_{CT} already accounts for non-idealities resulting within the heterojunction, we have introduced the factor, m, in Eq. 7 to account for nonradiative losses occurring *outside* the HJ. Depending on whether the m-factor is greater than or equal to 1, we establish that degradation primarily occurs outside of, or within the bulk active region, respectively.

We studied the vacuum-deposited DBP:C_{70} OPV devices with device structure: 150 nm ITO /10 nm MoO_3/54 nm DBP:C_{70} 1:8 BHJ/9 nm C_{70}/10 nm TPBi:C_{70}/3 nm TPBi/100 nm Al and were aged under 10, 18, and 27 sun. The degradation of V_{oc} and CT state EL intensity are shown in **Fig. 17 (a) and (b)**. The difference between the magnitude of the changes in EL and PCE during aging can be reconciled by fitting to the change in V_{oc} (ΔV_{oc}) to obtain m. The m-factor for DBP:C_{70} devices aged under 10 suns,18 suns, and 27 suns, **shown in Fig. 17 (c), (d) and (e)**, are

m_{10} = 1.030 ± 0.002, m_{18} = 1.010 ± 0.002, and m_{27} = 1.010 ± 0.003, which suggest that the non-radiative defect sites locates within the active region.

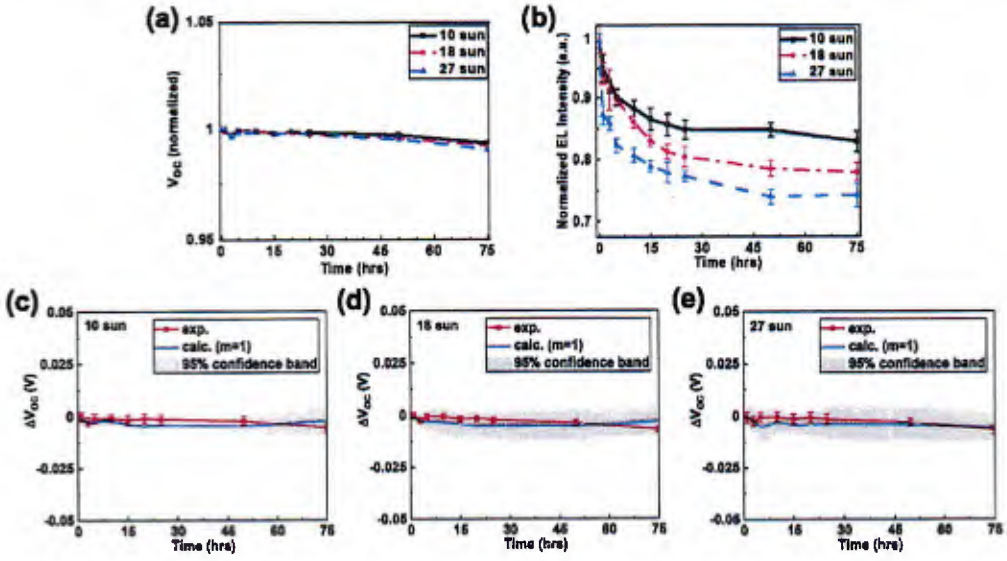

Figure 17. Normalized (a) V_{oc} and (b) peak EL intensity over time for vacuum-processed devices aged under 10, 18, and 27 sun white illumination. ΔV_{oc} over time for the devices aged under (a) 10 sun,(b) 18 sun, and (c) 27 sun.

In contrast to vacuum-processed devices, solution-processed devices have demonstrated performance instabilities over the short term. Here, we also studied the solution-processed PCE-10:BT-CIC devices with device structure: 150 nm ITO/30 nm ZnO/80 nm PCE10:BTCIC mixed BHJ/10 nm MoO_3/100 nm Al. To further investigate the non-idealities outside the BHJ, a C_{70}

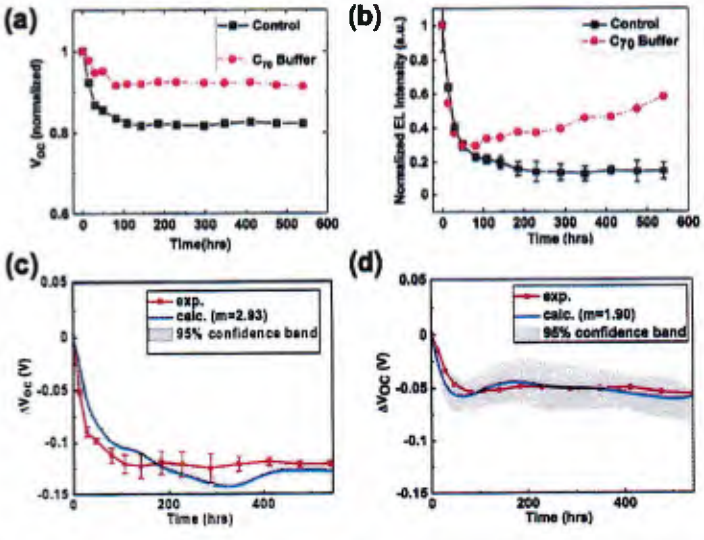

Figure 18. Normalized (a) V_{oc} and (b) peak EL intensity over time for solution-processed devices aged under simulated AM 1.5 G illumination at 1 sun intensity. ΔV_{oc} over time for (c) control and (d) C_{70} buffer solution-processed devices.

buffer structure with 2nm C_{70} between the BHJ and MoO_3 layer was also fabricated. **Figure 18 (a) and (b)** shows the degradation of V_{oc} and CT state EL intensity of the control devices and the C_{70} buffer devices. For these solution-processed devices, the best fit is found at $m = 2.93 \pm 0.09$ for the control and $m = 1.90 \pm 0.01$ for the C_{70} buffer structure, shown in **Fig. 18 (c) and (d)**. In this solution-processed OPV system, we observe that the inclusion of the buffer layer improves device lifetime. While the absolute value of m is not physically well-defined, a decrease in m in the C_{70} buffer structure relative to the control system indicates fewer nonidealities occurring outside of the heterojunction. In this case, the m-factors of the two systems confirm that the inclusion of a buffer layer in the solution-processed system is improving device performance by improving the stability outside of the heterojunction.

VI. Non-covalent interactions in near-infrared non-fullerene acceptors

NIR-absorbing NFAs have attracted extensive interest due to their contribution to high efficiency tandem solar cells and semitransparent devices. A challenge in developing efficient NIR acceptors is the tradeoff between driving force to charge separation, and voltage loss, which is particularly acute in narrow energy gap materials. A high V_{oc} requires that the acceptor have a high LUMO energy level, whereas a high HOMO energy level reduces the energy gap, E_g. However, the elevated HOMO of the acceptor diminishes the energy offset of the HOMOs between the donor and acceptor, which reduces the driving force and thus the photoinduced charge separation efficiency. Another challenge for NIR NFAs is a complex structure that requires multiple synthetic steps, leading to a high cost of materials.

Here, a simple NIR electron acceptor A078 was developed (see **Fig.19**). Compared to the isomer of SBT-FIC with seven fused rings, A078 with partially fused cores requires fewer synthetic steps, high yield and less toxic precursors, which enables A078 to be economically produced at large scale. Importantly, thin films of A078 exhibit significant bathochromic shifts of ~130 nm compared to SBT-FIC with an absorption peak at $\lambda_{max} = 900$ nm. Contrary to expectations, closer molecular packing leading to the spectral shifts is obtained when a rotation is imposed by the single bond between indaceno[1,2-b:5,6-b']dithieno[3,2-b]thiophene (IDT) and the flanking thiophene in A078.

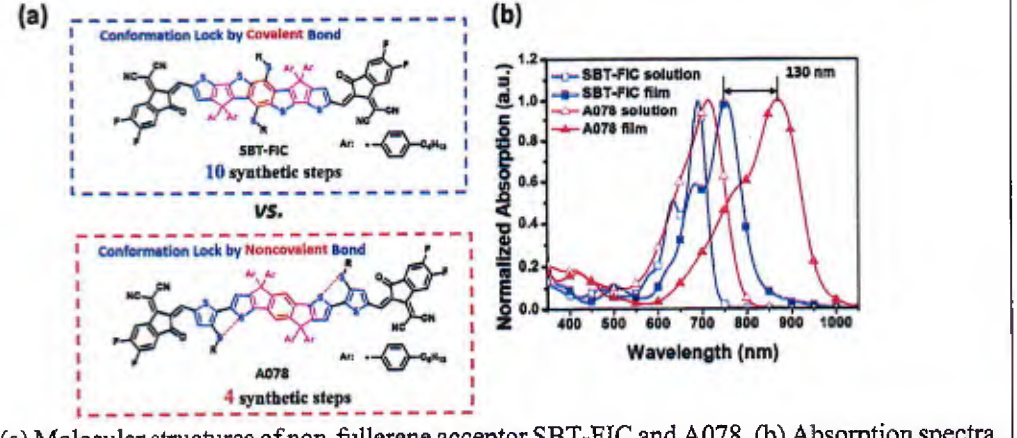

Figure 19. (a) Molecular structures of non-fullerene acceptor SBT-FIC and A078. (b) Absorption spectra for SBT-FIC and A078 in both solution and film states.

To understand the molecular conformation of A078, we conducted DFT calculations (**Fig. 20**). Within A078, two potentially rotatable single C–C bonds (center single bond between IDT

and thiophene; terminal single bond between thiophene and acceptor capping) were available. The relaxed potential surface energy scans of possible rotamers were performed. The energy–torsion angle curves (E–θ curves) reveal that center rotamer has two favorable conformations with the lowest total energy (180° rotamer featured with S–S interaction and 20° rotamer featured with S–H interaction). Note that the S–S geometry has a slightly lower total energy than that of the S–H geometry. In addition, the E–θ curves of the terminal C–C bond were investigated. The terminal rotamer has only one favorable conformation at 180° with the lowest total energy (180° rotamer featured with O–H interaction and 0° rotamer featured with S–O interaction). However, if we change the alkythiol chain on the flank thiophene unit into alky chain, the center rotamer becomes only one favorable conformation. **Figure 20** shows that the S···S distance between 2-ethylhexanethiol group on the thiophene and the IDT (3.18 Å) unit is far shorter than the sum of the van der Waals radii of the two sulfur atoms (3.68 Å). This reveals that noncovalent S···S interactions rigidify the conjugated structure, resulting in a reduction of the torsion angle between the thiophene and IDT from 20° to 2.5°.

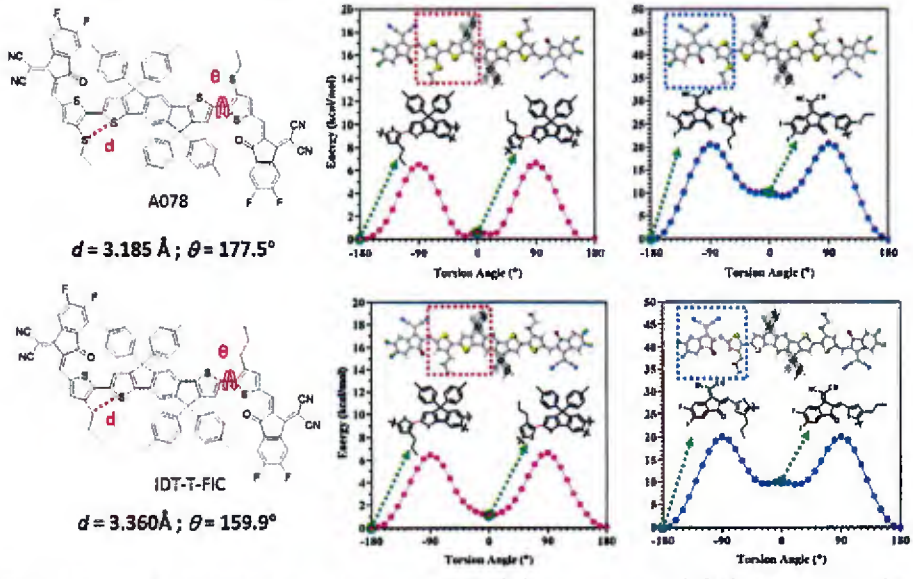

Figure 20. Calculated molecular geometry and a possible rotamers and their energy–torsion angle (E–θ) curves of the non-fullerene acceptors from density functional theory using the TZP (triple zeta polarized set) basis set at the G GA (generalized gradient approximation) level.

The NFAs blended with PCE-10 were employed in OPVs with the structure: ITO/ZnO (30 nm) /Active layer (~100 nm) /MoO_3 (20 nm) /Ag (100 nm). Their $J-V$ characteristics are plotted in **Fig. 21**. Here, PCE = 13.0±0.4 % is achieved in the A078-based device, with V_{OC} = 0.75 ± 0.01 V, J_{SC} = 24.8 ± 0.7 mA cm^{-2}, and FF = 0.70 ± 0.04. In contrast, the SBT-FIC-based OPV exhibited PCE = 7.8 ± 0.3% with V_{OC} = 0.70 ± 0.01 V, J_{SC} = 17.2 ± 0.7 mA cm^{-2}, and FF = 0.65 ± 0.02. **Figure 21(b)** shows the external quantum efficiency (EQE) spectra of these devices. The significant improvement in J_{SC} for the A078 compared to the SBT-FIC OPV is attributed to its ~200 nm absorption red-shift that provides solar spectral coverage further into the NIR. Interestingly, the EQE of the A078 OPV reaches 80%, between λ = 700 nm and 900 nm, while leaving a transparency window between the visible wavelengths of 400 nm and 650 nm.

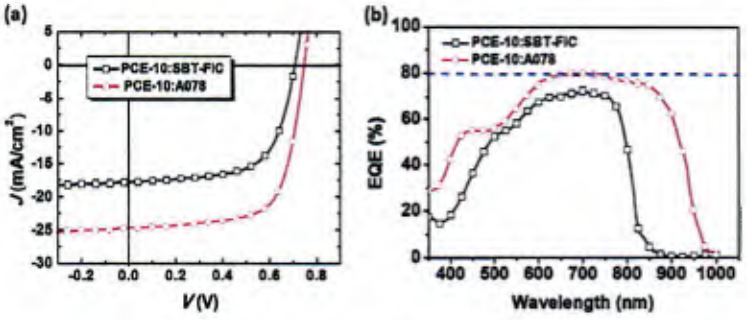

Figure 21. (a) *J-V* characteristics, and (b) external quantum efficiency (*EQE*) spectra of OPV cells based on PCE-10: SBT-FIC and PCE-10:A078.

Training Opportunities

Along with an Assistant Research Scientist, one (now) post-doctoral student, three graduate students and one undergraduate student participated in the research for this project.

Results Dissemination

Peer reviewed publications have been written and talks presented at technical conferences as listed in the Products section below.

Honors and Awards

2017: IEEE Jun-ichi Nishizawa Medal, Stephen R. Forrest
2018: Elected to American Academy of Arts and Sciences, Stephen R. Forrest
2018: Honorary PhD, The Technion, Israel Institute of Technology, Stephen R. Forrest

Technology Transfer

UM 2019-333 Asymmetrical Non-Fullerene Acceptor Molecules, disclosed 3/6/19
Inventors: Stephen R. Forrest and Yongxi Li
U.S. Application No. 16/903,874 filed 6/17/20

UM 2019-253 Acceptor bottom layer for organic photovoltaics, disclosed 1/24/19
Inventors: Stephen R. Forrest and Kan Ding
U.S. Application No. 16/937,128 filed 7/23/20

UM 7775 Adjusting donor-acceptor group distances to reduce the energy loss in organic solar cells, disclosed 10/30/17
Inventors: Stephen R. Forrest, Yongxi Li and Xiao Liu
U.S. Application No. 16/761,914 filed 5/6/20

UM 7588 Near-Infrared non-fullerene electron acceptors for high performance polymer solar cells, disclosed 6/7/17
Combined with UM7775 above

UM 7415 High efficiency single junction non-fullerene acceptor based semi-transparent solar cells, disclosed 3/1/17
U.S. Provisional Patent Application No. 62/582,212 filed 11/6/17
Combined with UM7775 above

Participants

Stephen Forrest – Principal Investigator
Yongxi Li – Assistant Research Scientist
Dejiu Fan – Post Doctoral Fellow
Xiaheng Huang, Xiao Liu, Kan Ding, Xinjing Huang, Xiaozhou Che – Graduate Student
Fanhao Zeng – Undergraduate Student

Students

Number of students receiving STEM degrees during the reporting period: 3
Number of undergraduate and graduate STEM participants during the reporting period: 4

Publications

"Reducing Energy Losses at the Organic–Anode-Buffer Interface of Organic Photovoltaics," K Ding, SR Forrest, *Physical Review Applied*, **13** (5), 054046, 19 May 2020, https://doi.org/10.1103/PhysRevApplied.13.054046

"A 3D Nonfullerene Electron Acceptor with a 9, 9'-Bicarbazole Backbone for High-Efficiency Organic Solar Cells," C Jiang, X Huang, B Sun, Y Li, M Gao, L Ye, H Ade, SR Forrest, J Fan, *Organic Electronics*, **84**, 2020, 105784, https://doi.org/10.1016/j.orgel.2020.105784

"15.9% Organic Tandem Solar Cell with Extended Near-Infrared Absorption," X Huang, B Sun, Y Li, C Jiang, D Fan, J Fan, SR Forrest, *Applied Physics Letters*, **116** (15), 153501

"Vacuum-Deposited Bilayer Ternary Organic Photovoltaics," *JACS*, 2019, **141**,45, 18204-10, DOI: 10.1021/jacs.0b09012

"Is there such a thing as a molecular organic alloy?" Xinjing Huang, Xiao Liu, Kan Ding and Stephen R. Forrest, *Materials Horizons*, 2020, 7, 244-251, DOI 10.1039/c9mh01351b

"Intrinsically stable organic solar cells under high-intensity illumination," Q Burlingame, X Huang, X Liu, C Jeong, C Coburn, SR Forrest, *Nature*, **573**, 394-7 (2019)

"Engineering Charge-Transfer States for Efficient, Low-Energy-Loss Organic Photovoltaics," X Liu, BP Rand, SR Forrest, *Trends in Chemistry*, https://doi.org/10.1016/j.trechm.2019.08.001

"Enhanced Light Utilization in Semitransparent Organic Photovoltaics Using an Optical Outcoupling Architecture," Y Li, C Ji, Y Qu, X Huang, S Hou, CZ Li, LS Liao, LJ Guo, SR Forrest, *Advanced Materials*, **31**, 40, October 4, 2019, 1903173, https://doi.org/10.1002/adma.201903173

"Near-Infrared Ternary Tandem Solar Cells," Y. Li, J.D. Lin, X. Liu, Y. Qu, F.P Wu, F. Liu, Z.Q. Jiang, and S.R. Forrest, *Advanced Materials*, **30** (45) 1804416, 2018. DOI: 10.1002/adma.201804416

"Energy Loss in Organic Photovoltaics: Nonfullerene Versus fullerene acceptors," X. Liu, Y. Li, K. Ding and S.R. Forrest, *Phys. Rev. App.*, **11**, 024060 (2019).

"High Fabrication Yield Organic Tandem Photovoltaics Combining Vacuum- and Solution-Processed Subcells with 15% Efficiency," X. Che, Y. Li, Y. Qu and S.R. Forrest, *Nat. Energy*, **3**, 422-7 (2018). https://doi.org/10.1038/s41560-018-0134-z

"Charge Transfer and Collection in Dilute Organic Donor–Acceptor Heterojunction Blends" K. Ding, X. Liu, S. R. Forrest, *Nano Letters*, **18**, 3180-4, DOI: 10.1021/acs.nanolett.8b00851 (2018).

"High Efficiency Near-infrared and Semi-transparent Non-Fullerene Acceptor Organic Photovoltaic Cells", Y. Li, J.-D. Lin, X. Che, Y. Qu, F. Liu, L.-S. Liao, and S. R. Forrest, *J. Am. Chem. Soc.*, DOI: 10.1021/jacs.7b11278, **139** 17114 (2017).

"Isomeric Effects of Solution Processed Ladder-Type Non-Fullerene Electron Acceptors" Y. Li, L. Zhong, J.-D Lin, F.-P. Wu, H.-J. Bin, Z. Zhang, L. Xu, Z.-Q. Jiang, Z.-G. Zhang, F. Liu, T. P. Russell, Y. Li, L.-S. Liao, S. R. Forrest, *Solar RRL*, DOI: 10.1002/solr.201700107, **1** (2017).

Presentations

Xiao Liu, "Low energy loss photogeneration of organic photovoltaics using non-fullerene acceptors." SPIE Conference, San Diego, CA. August 18 – 24, 2018

Yongxi Li, "Ternary organic solar cells with small voltage losses." SPIE Conference, San Diego, CA. August 18 – 24, 2018

S.R. Forrest, "Charge transfer states at donor-acceptor heterojunctions: The role of morphology on dissociation efficiency and device lifetime." ONR OPV Program Review, Altanta, GA. September 20, 2018.

Xinjing Huang, "Alloy or blend: Analysis of a ternary organic photovoltaic." APS Spring Meeting, Boston, MA. March 3 – 10, 2019.

S.R. Forrest, "Charge transfer states at donor-acceptor heterojunctions: The role of morphology on dissociation efficiency and device lifetimes." ONR Organic and Hybrid Perovskite Photovoltaics Peer Review, Golden, CO. April 15 – 16, 2019.

Yongxi Li, "Enhanced light utilization efficiency from semi-transparent organic photovoltaics using an outcoupling architecture," IEEE PVSC 46, Chicago, IL. June 16 – 21, 2019.

K. Ding, "Role of morphology in exciton dissociation and charge extraction in dilute donor-acceptor blend organic heterojunctions," SPIE Optics and Photonics, Paper 10363-102, San Diego (8-10 Aug., 2017).

Yongxi Li, "Chlorinated Non-Fullerene Acceptors for High Performance Near Infrared Semitransparent Solar Cells", and S. R. Forrest, Mat. Res. Soc. Ann Mtg. Paper EM01.10.60, Boston (Nov., 2017)